Cooperative Organization in Iron Oxide Multi-Core Nanoparticles Potentiates Their Efficiency as Heating Mediators and MRI Contrast Agents

Lénaic Lartigue,[†] Pierre Hugounenq,[‡] Damien Alloyeau,[§] Sarah P. Clarke,[∥] Michael Lévy,[†] Jean-Claude Bacri,[†] Rana Bazzi,[‡,⊥] Dermot F. Brougham,[∥] Claire Wilhelm,[†] and Florence Gazeau[†,*]

[†]Laboratoire Matières et Systèmes Complexes, UMR 7057 CNRS/Université Paris Diderot, 10 rue Alice Domon et Léonie Duquet, 75013 Paris, France, [‡]Laboratoire Physico-Chimie des Electrolytes, Colloïdes et Chimie Analytique, UMR 7195 CNRS/Université Pierre et Marie Curie/ESPCI, 4 place Jussieu, F-75252 Paris Cedex 05, France, [§]Laboratoire Matériaux et Phénomènes Quantiques, UMR 7162 CNRS/Université Paris Diderot, 10 rue Alice Domon et Léonie Duquet, F-75205 Paris Cedex 13, France, [⊥]Institut UTINAM, UMR 6213 CNRS/Université de Franche-Comté, 16 route de Gray, 25030 Besançon, France, and [∥]National Institute for Cellular Biotechnology, School of Chemical Sciences, Dublin City University, Dublin 9, Ireland

ABSTRACT

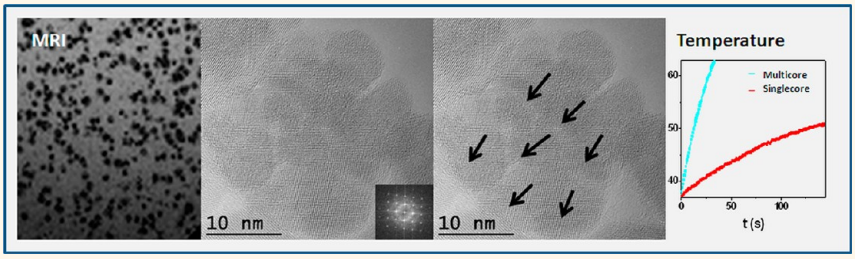

In the pursuit of optimized magnetic nanostructures for diagnostic and therapeutic applications, the role of nanoparticle architecture has been poorly investigated. In this study, we demonstrate that the internal collective organization of multi-core iron oxide nanoparticles can modulate their magnetic properties in such a way as to critically enhance their hyperthermic efficiency and their MRI T_1 and T_2 contrast effect. Multi-core nanoparticles composed of maghemite cores were synthesized through a polyol approach, and subsequent electrostatic colloidal sorting was used to fractionate the suspensions by size and hence magnetic properties. We obtained stable suspensions of citrate-stabilized nanostructures ranging from single-core 10 nm nanoparticles to multi-core magnetically cooperative 30 nm nanoparticles. Three-dimensional oriented attachment of primary cores results in enhanced magnetic susceptibility and decreased surface disorder compared to individual cores, while preserving a superparamagnetic-like behavior of the multi-core structures and potentiating thermal losses. Exchange coupling in the multi-core nanoparticles modifies the dynamics of the magnetic moment in such a way that *both* the longitudinal and transverse NMR relaxivities are also enhanced. Long-term MRI detection of tumor cells and their efficient destruction by magnetic hyperthermia can be achieved thanks to a facile and nontoxic cell uptake of these iron oxide nanostructures. This study proves for the first time that cooperative magnetic behavior within highly crystalline iron oxide superparamagnetic multi-core nanoparticles can improve simultaneously therapeutic and diagnosis effectiveness over existing nanostructures, while preserving biocompatibility.

KEYWORDS: multi-core nanoparticles · exchange coupling · magnetic nanoparticles · hyperthermia treatment · MRI contrast agent

Iron oxide nanoparticles continue to emerge as one of the most powerful nanomaterials for biomedical applications. A key advantage is that multiple functionalities arise from their responsiveness to external magnetic stimuli. Superparamagnetic nanoparticles are efficient contrast agents for magnetic resonance imaging (MRI) owing to their strong and reversible magnetization under constant field. Submitted to an alternating field, they are also potent heating mediators that can be used for hyperthermic cancer treatment,[1] for thermally activated drug release,[2] or for remote activation of cell functions.[3] In the presence of a magnetic field gradient, they enable magnetic targeting and manipulation of therapeutic vectors and cells. Thus by combining detectability,

* Address correspondence to florence.gazeau@univ-paris-diderot.fr.

Received for review September 27, 2012 and accepted November 20, 2012.

Published online November 20, 2012
10.1021/nn304477s

© 2012 American Chemical Society

on-command remote actuation, and therapeutic properties, they are perfect examples of the recently defined theragnostic agents.[4−7] However, many challenges remain in order to optimize the magnetic properties of nanostructures for combined hyperthermia treatment, MRI monitoring, and magnetic targeting, while maintaining biocompatibility, degradability, and control over their distribution and fate in the organism.

In the last decades, there have been many attempts to control the magnetic properties of nanoparticles by tuning their size,[8] magnetic anisotropy,[9] and magnetization,[10] which are the parameters identified by theoretical studies as the determinants of both the static and dynamic behavior of single-domain nanoparticles. In particular, the so-called linear response theory describes the size and anisotropy dependencies of their thermal losses[11] and MR relaxivities[12] by considering Néel fluctuations of the magnetic moment within the crystal lattice and Brownian fluctuations of the particle itself. While this description is quite satisfactory for single-core nanoparticles in the 5−18 nm size range,[13,14] unexpected properties have been discovered by varying the internal structure and organization of nanomagnets. For example, core−shell nanostructures, prepared by selectively doping ferrite phases, exhibited exchange coupling between the magnetically soft shell and magnetically hard core. This led to unprecedented hyperthermic potency, which could potentially improve magnetically based cancer therapy.[9] However, doping nanoparticles with potentially toxic metals raises important concerns regarding their fate in the organism. Iron oxide has been shown to be degraded and safely assimilated in the body,[15] so it is still preferred for biomedical applications. Recently, the modulation of nanoparticle shape was shown to enhance both heating power (measured by the specific absorption rate, SAR) and MRI relaxivities.[16,17] Biogenic magnetosomes extracted from bacteria,[18] chemically synthesized iron oxide nanocubes,[17,19] and nanoflowers[20,21] exhibit some of the highest reported SAR values to date; interestingly, these materials all exhibited behavior close to the transition between superparamagnetism and ferrimagnetism.[22] Moreover, the external organization of nanoparticles, such as their ability to form linear assemblies or isotropic clusters, can profoundly influence their magnetic behavior.[23,24] However, the influence of nanoparticle architecture and internal magnetic order on the emergent magnetic properties is still not understood.

In this paper, we show that multiple iron oxide cores, formed as magnetically cooperative multi-core nanoparticles, potentiate magnetic properties for both MRI and hyperthermia applications. By combining a polyol synthetic approach with electrostatic colloidal sorting, we were able to modulate magnetic interactions in citrate-stabilized suspensions, ranging from 10 nm single-core to cooperative 30 nm multi-core nanoparticles. We show that the iron oxide cores can coalesce with a common orientation such that both the crystallographic and the magnetic order continue across the interface, leading to enhanced susceptibility and decreased surface disorder and anisotropy. By tuning the architecture and magnetic properties, we highlight the role of collective magnetic behavior in multi-core superparamagnetic nanostructures for enhancing both heating power and MR relaxivities. Moreover, with no need for any substrate matrix, the citrate-coated multi-core nanoparticles present high colloidal stability and are quickly, efficiently, and safely internalized by tumor cells. Their efficacy for killing breast cancer cells by magnetic hyperthermia and for detection by MRI even after several cell divisions is demonstrated. This study highlights for the first time the role of internal structure in colloidal superparamagnetic nanoparticles in generating collective magnetic properties that critically improve therapeutic and diagnostic values of biocompatible iron oxide nanomaterials.

RESULTS AND DISCUSSION

Synthesis of Multi-Core Nanoparticles and Colloidal Size Sorting. We synthesized multi-core (MC) maghemite, γ-Fe_2O_3, nanoparticles using a single-step high-temperature hydrolysis approach. The first synthesis used a stoichiometric mixture of two polyol solvents, diethylene glycol (DEG) and *N*-methyldiethanolamine (NMDA), 1/1 by weight as previously described.[20,25] The mixture was stirred at room temperature for 3 h, followed by a linear temperature ramp until 220 °C and was then stirred for 12 h at constant temperature, 220 °C. The heating ramp and high temperature hold period have been shown previously to allow clustering and coalescence of the preformed seeds, respectively.[20,26] The particles were fully oxidized into maghemite to ensure their chemical stability by a forced oxidation using an iron nitrate solution. This procedure yielded monodisperse multi-core flower-like nanostructures (MC0) with a mean size of 24.9 nm (Figure 1, Table 1), which were stable in water at acidic pH. To compare the properties of the multi-core to single-core particles, we modified the synthesis in order to obtain multi-core nanoparticles coexisting with smaller sized single-core particles in a single preparation. This was achieved by using a nonstoichiometric DEG/NMDA mixture (0.33/0.66). To separate the different populations of nanostructures in the acidic medium, we induced phase separation by increasing the ionic strength of the suspension.[13,27] As the phase diagram depends on particle size,[28] a succession of controlled phase separations allowed fractionation of the initial distribution of the colloid. Three successive phase separations (see Supporting Information, Figure S1) resulted in four fractions, three of which contained nearly monodisperse multi-core nanoparticles with a mean size of 19.6, 22.2, and 28.8 nm (named MC3, MC2, and MC1,

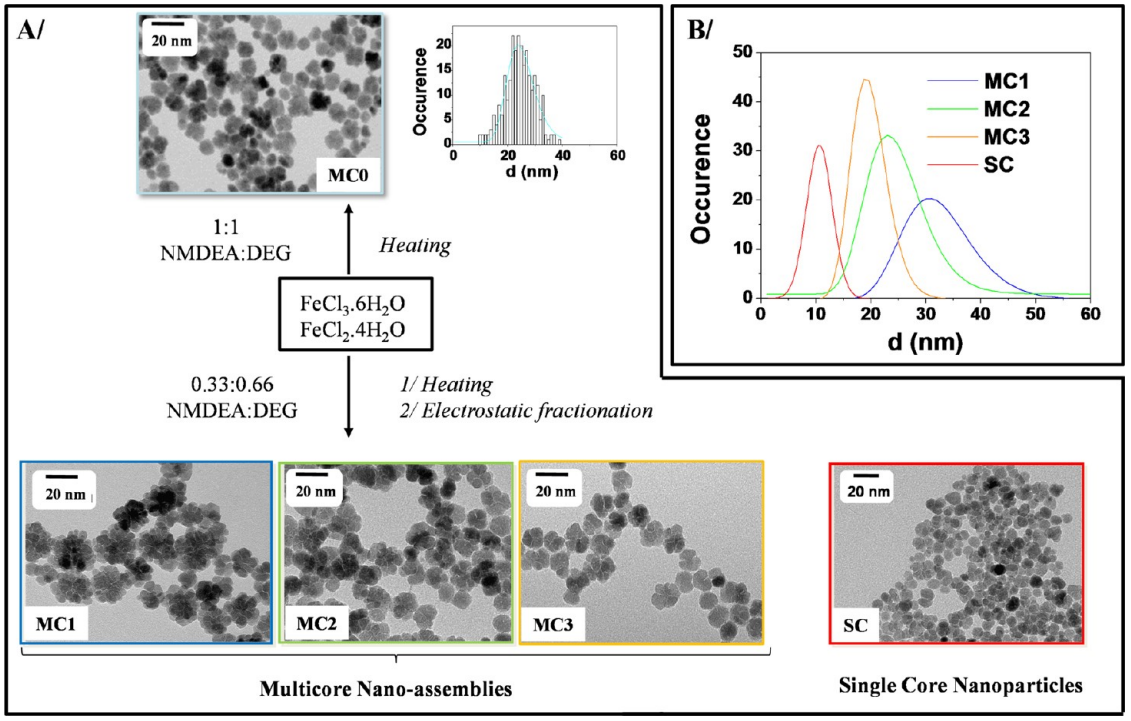

Figure 1. (A) Procedure for the synthesis of the different samples with a polyol route; MC0 is realized using a stoichiometric mixture of two polyols. The others samples are issued from electrostatic size sorting of a polydisperse suspension obtained using a mixture of NMDEA/DEG at a ratio of 0.33:0.66. (B) TEM size distribution of each sample calculated by measuring 300 particles in each case.

TABLE 1. Zeta-Potential (ζ) and Average Size of Nanostructures Determined by TEM, XRD, and DLS

	TEM[a]			XRD	DLS		
	d_{TEM} multi- core (nm)	σ	d_{TEM} core (nm)	d_{XRD} (nm)	d_{HYD} (nm)	PDI[b]	ζ-potential (mV)
MC0	24.0	0.18	10.5	15.6	37.0	0.20	−76.0
MC1	28.8	0.19	8.5	12.0	38.5	0.12	−71.3
MC2	22.2	0.22	7.5	13.5	44.3	0.23	−70.0
MC3	19.7	0.17	7.1	11.0	27.0	0.16	−64.9
SC	10.3	0.30	10.3	9.2	77.6	0.19	−72.6

[a] The TEM size distribution follows a log-normal distribution with a characteristic diameter (d_{TEM}) and standard deviation (σ). [b] Polydispersity index determined by DLS.

respectively) and one containing monodisperse single-core nanoparticles of 10.3 nm (SC) (Figure 1, Table 1). Note that our size-sorting process effectively removes any larger aggregates. This approach yields single-core and multi-core nanoparticles from the same synthesis conditions, thus allowing a reliable comparison of their magnetic properties and avoiding bias due to different preparations.

For both procedures, the resulting aqueous dispersions were stable in acidic or basic conditions, with the isoelectric point near pH 7. The colloidal stability at biological pH was thus ensured by adsorption of hydrophilic citrate anions on the surface of MC and SC particles. This was confirmed by dynamic light scattering (DLS) and zeta-potential measurements showing monodisperse distribution for the multi-core structures (PDI index <0.23) with mean hydrodynamic diameters, d_{HYD}, very close to their size extracted from transmission electron microscopy (TEM) and isoelectric point close to 3 (Table 1). The electrostatic fractionation approach followed by citrate coating provides stable suspensions of multi-core nanoparticles in physiological media (water or Roswell Park Memorial Institute, RPMI, cell culture medium), combined with a very tight control over their size and structure up to 30 nm. It is important to note that the d_{HYD} values were unchanged following exposure to a magnetic field up to 1.5 T, confirming that citrate-induced electrostatic repulsion counterbalances attractive dipole−dipole interparticle interactions.

Structural Characterization: From Single-Core to Cohesive Multi-Core Nanoparticles. Bright-field TEM electron tomography revealed the three-dimensional arrangement of the nanoparticles (Figure 2). In the bright-field images, acquired with a tilt angle of −60, 0, and +60° (Figure 2A−C), the multigrain structure of the nanoparticles and the rugosity of their surfaces can be easily distinguished. A three-dimensional reconstruction is presented in Figure 2D. Tomography permits extraction of 2D slices from the 3D reconstruction,[29,30] providing better understanding of the complex nanoflower structure. Two slices, parallel (Figure 2E) and perpendicular (Figure 2F) to the substrate, highlight the porosity; the white contrast reveals the presence of voids inside the

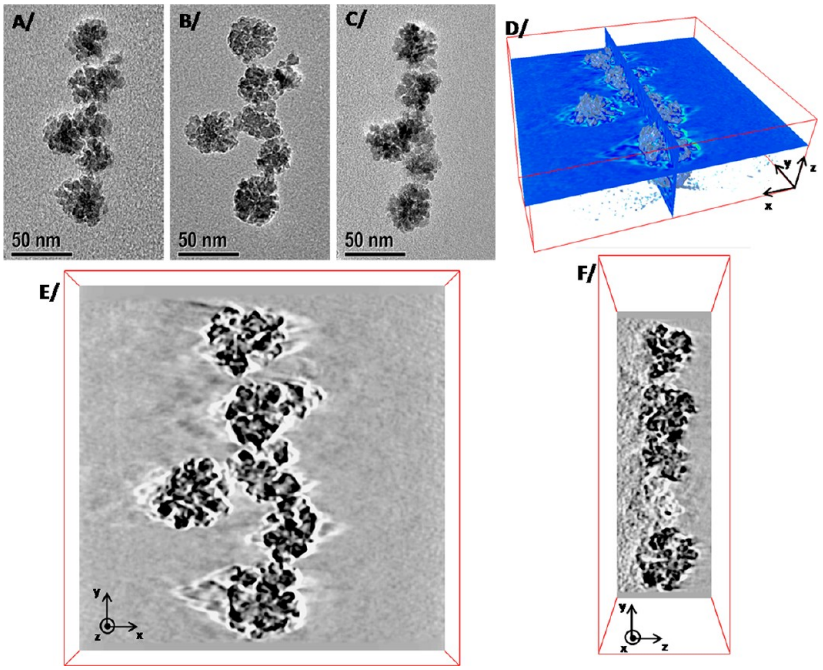

Figure 2. Three-dimensional analysis of the MC0 maghemite nanoparticles by bright-field TEM tomography. Bright-field images acquired with a tilt angle of (A) −60, (B) 0, and (C) +60°. (D) Three-dimensional representation of the particles (tomogram). Two-dimensional slices extracted from the tomogram: (E) 2D slice parallel to the substrate, corresponding to the blue (*x*,*y*) plane in the 3D representation; (F) 2D slice perpendicular to the substrate, corresponding to the blue (*y*,*z*) plane in the 3D representation.

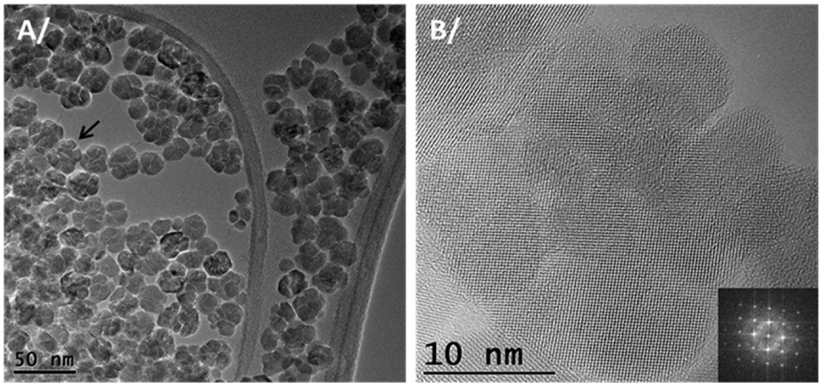

Figure 3. (A) Bright-field TEM image of the MC0 maghemite nanoparticles deposited on a lacey TEM grid. (B) Aberration-corrected high-resolution image of the particle marked out with an arrow in (A). The Fourier transform of this HRTEM image (inset) confirms the single-crystal structure of the MC nanoparticle.

nanoparticles. It is clear that the nanoflowers consist of an assembly of merged cores sharing a same facet. As shown in Figure 2F, the diameter in the substrate plane (*y* direction) is always very close to the diameter perpendicular to the substrate (*z* direction). We can conclude from electron tomography that the nanoflowers are isotropic assemblies of cores, forming nearly spherical porous supercrystals, with the overall diameter depending on the number of cores present.

The atomic structure of the nanoflowers was characterized by aberration-corrected high-resolution TEM and X-ray diffraction (XRD). For the TEM experiments, nanoparticles were deposited on a lacey grid in order to observe the nanocrystals over the vacuum (Figure 3A). Surprisingly, most of the multi-core nanoparticles are single crystals. In Figure 3B, the continuity of the crystal lattice at the grain interfaces can be clearly observed. The Fourier transform of this high-resolution image (see inset) unambiguously shows the monocrystalline face-centered cubic (fcc) structure of the multi-core nanoparticles, oriented along the [001] zone axis. This suggests that individual cores have rotated during the ripening phase at high temperature to share the same crystal orientation, minimizing their surface energy.[26,31] However, as previously reported,[20] fine analyses of HRTEM images reveal small rotations from 1 to 2° of the crystalline structure between the individual cores of the nanoflowers (Supporting Information, Figure S2).

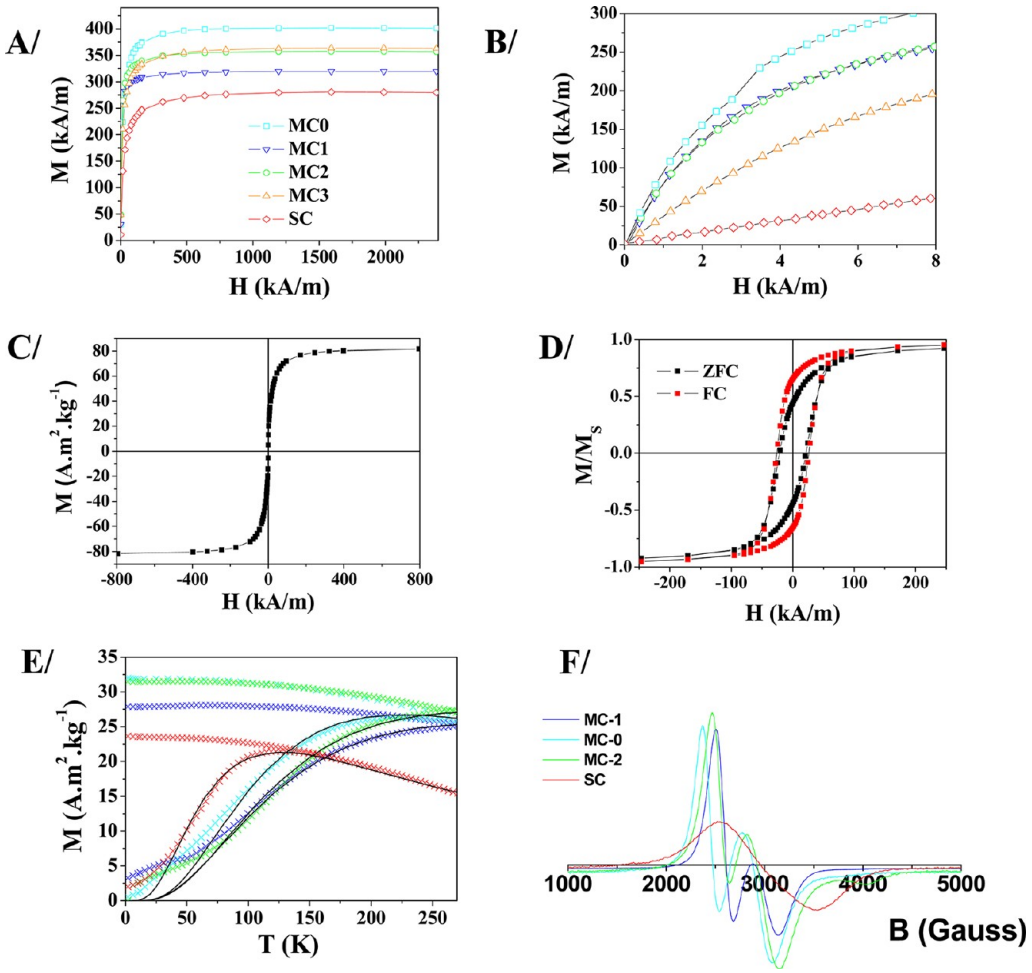

Figure 4. Magnetic measurement performed on aqueous suspension for MC0 (cyan), MC1 (blue), MC2 (green), MC3 (orange), and SC (red) at a concentration of iron of 10 mM. (A) First magnetization curve realized at 310 K, in $A \cdot m^2 \cdot kg^{-1}$ of magnetic material. (B) Initial magnetization at low field measured at 310 K. (C) Field-dependent magnetization cycle at 310 K for MC0, showing no hysteresis. (D) Field-dependent magnetization cycles for MC0 at 5 K under ZFC and FC conditions (HFC = 2390 kA/m). (E) Field-cooled and zero-field-cooled magnetization (FC/ZFC) *versus* temperature curves performed with an applied field of 4 kA/m. The black solid lines represent the fits of the ZFC. Details for the fitting as well the deduced anisotropy and magnetic size are summarized in the Supporting Information. (F) Ferromagnetic resonance spectra of the different samples at 9.25 GHz.

In good agreement with TEM structural investigations, XRD patterns (Supporting Information, Figure S3) are consistent with the γ-Fe_2O_3 crystalline structure. For the single-core nanoparticles, the mean crystallite diameter deduced from peak broadening using Scherrer equation, d_{XRD}, of 9.2 nm was in good agreement with the d_{TEM} value of 10.3 nm. However, for the multi-core nanoparticles, d_{XRD} ranged from 9.2 to 15.6 nm, which is significantly smaller in all cases than the TEM size (which ranged from 10.3 to 28.8 nm, Table 1) and larger than the apparent TEM size of the cores. The difference between the XRD and TEM values could be explain by the minor crystal structure misalignments at the core interface revealed by high-resolution imaging.[20,26,31]

Nitrogen adsorption measurements also confirmed the cohesive, but porous, structure of the nanoparticles: a specific surface area of 82 m^2/g was found for MC1 sample, which is 2 times higher than that of a sphere of same diameter (28.8 nm) and 20% smaller the specific surface area of the 12 nm cores (Supporting Information, Figure S4).

Cooperative Magnetic Behavior of Multi-Core Nanostructures. The next step was to shed light on how the highly ordered internal structure of multi-core nanoparticles affects their magnetic properties. Magnetization measurements were first performed at 310 K in water, as a function of the applied magnetic field up to 3 T (Figure 4A). Saturation magnetization, M_s, values were close to that for bulk maghemite (80 $A \cdot m^2 \cdot kg^{-1}$ of magnetic materials) for all samples except for the single-core 10 nm nanoparticles, which show a 30% diminution with respect to the bulk value (Table 2). In parallel, the initial susceptibility of the suspensions, χ_0, also increased with increasing d_{TEM} for the size-selected multi-core samples (Figure 4B). The larger susceptibility was found, however, for the monodisperse sample MC0 obtained using the first synthesis

TABLE 2. Magnetic Characteristics of Nanostructures

sample	T_{max} (K)[a]	M_s (5 K) (A·m^2·kg^{-1})	M_s (310 K) (A·m^2·kg^{-1})	M_r/M_s (5 K)	H_C (5 K) (kA/m)	χ_0	μ_{eff} ($\times 10^{-9}$ A·m^2)
MC0	219	83.6	81.8	0.45	21.5	5.3	5.1
MC1	>270	76.9	65.4	0.43	17.1	4.9	5.7
MC2	260	84.3	73.9	0.43	17.9	4.9	3.8
MC3	230	88.7	72.9	0.36	26.3	2.3	2.2
SC	120	72.3	57.5	0.41	21.7	0.6	0.6

[a] T_{max} is temperature where the maximum value for the magnetization in the ZFC curve is reached.

procedure. From the measured values of initial susceptibility χ_0, one can calculate an effective magnetic moment, μ_{eff}, for the nanostructure (Table 2) according to the relation $\chi_0 = (\mu_0/V_{tot})(\mu_{eff}^2/3k_BT)$,[23] where V_{tot} is the nanoparticle volume. Remarkably, the μ_{eff} values were enhanced in multi-core as compared to single-core structures, suggesting collective magnetic behavior of the cores. No hysteresis was found at room temperature, confirming the rotational mobility of individual multi-core nanoparticles in suspension (Figure 4C). This is consistent with DLS measurements which show that multi-core nanoparticles remained dispersed even after exposure to magnetic fields. Hence the magnetization curves reveal *intraparticle* collective behavior, which enhances the effective particle magnetic moment, and demonstrates the absence of *interparticle* magnetic interactions, which could compromise the superparamagnetic properties and indeed the colloidal stability of the suspension at room temperature.

To highlight the behavior of multi-core nanoparticles, we carried out a systematic study of their field- and temperature-dependent magnetic properties in gelatin to avoid strain due to crystallization of the aqueous liquid carrier and to minimize dipole−dipole interactions between the particles. Field-dependent magnetization curves measured at 5 K upon 3 T field cooling (FC) and zero field cooling (ZFC) displayed the same coercivity and saturation magnetization and were symmetric with respect to the origin, demonstrating the absence of exchange bias for all of the samples (Figure 4D). This observation rules out the presence of distinct magnetic phases at the interfaces between cores. Exchange bias phenomena are observed when magnetic interfaces in intimate contact show different magnetic behavior (typically ferromagnetic−antiferromagnetic) or different magnetic disorder (antiphase boundaries, spin canting, or spin glass, for example). Exchange bias was recently observed in core−shell maghemite nanoparticles synthesized by a seeded-growth method, and the effect was attributed to disorder at the interface.[32] For nanoflowers, the absence of exchange bias is consistent with continuity of the magnetic order at the grain interface arising due to the shared crystallographic orientation demonstrated by TEM.

Magnetization curves recorded at 5 K show that the coercive fields changed only slightly when varying the structure of nanoparticles (Table 2, Supporting Information, Figure S5). Also the reduced remanence (M_r/M_s) increased from 0.41 for single-core to 0.5 for the largest multi-core sample. However, the temperature dependence of the low-field FC and ZFC magnetization was drastically different for MC with respect to SC nanoparticles; we observed both enhanced magnetization and a severe increase of the blocking temperature (maximum of the ZFC curve) for MC nanoparticles (Figure 4E). It should be noted that, for all samples, the temperature of irreversibility (where FC and ZFC curves meet) was close to the blocking temperature, suggesting that dipole−dipole interparticle interactions and size polydispersity do not play a prominent role in the magnetic behavior. The temperature dependence of ZFC magnetization could be fitted using the classical theory for superparamagnetic nanoparticles taking into account the Néel thermal fluctuations of polydisperse individual magnetic moments (see theory appendix in Supporting Information). We could extract the anisotropy constant K and the effective magnetic size distribution (described by a log-normal distribution with a characteristic magnetic diameter d_0 and polydispersity index σ) for each sample (Table 3). First, the anisotropy constant was found to be significantly larger for single-core (2.6×10^4 J/m^3) as compared to multi-core nanoparticles ($1.75-2.5 \times 10^4$ J/m^3). Second, the effective magnetic diameter clearly increased from 10.6 nm for SC to 13.3−15.0 nm for MC (with polydispersity index increasing from 0.21 to 0.25). Increased magnetic diameter is entirely consistent with both the enhancement of μ_{eff}, at room temperature, and the increase in d_{XRD} for multi-core nanoparticles. This indicates that our multi-core materials do not behave magnetically as the individual cores, but rather show enhanced magnetic properties, as revealed by larger apparent magnetic size and reduced anisotropy.

TABLE 3. Parameters Used To Fit the ZFC Curves of Nanostructures[a]

sample	d_0 (nm)	σ	$K \times 10^4$ (J/m^3)
MC0	14.0	0.25	1.75
MC1	14.8	0.24	1.90
MC2	15.0	0.23	1.80
MC3	13.3	0.23	2.50
SC	10.6	0.21	2.60

[a] For the calculation, we fixed $\tau_0 = 10^{-9}$ s.

To understand this unusual behavior, we should consider the different types of interactions which may take place within multi-core magnetic nanoparticles. First, dipole−dipole interactions may have a significant effect on the dynamic processes. When the dipole−dipole interaction energy becomes larger than thermal fluctuations, dipolar interactions can result in ordering of the moments. However, the subsequent organization and collective magnetic behavior may differ depending on whether individual cores can move freely or not. In some cases, as for magnetosomes observed in bacteria, there is a tendency to form linear chains of nanoparticles with each magnetic moment oriented in the chain direction,[33] and closed rings have also been observed.[34]

For weaker dipolar interactions, or for immobilized nanoparticles in a cluster, the interacting magnetic cores may form a "dipole glass" or "super-spin glass" with similar magnetic properties to those of spin glasses.[35−38] Numerical simulations indicate that the global (static) magnetization of the cluster is decreased by dipolar interactions.[23,24,39] In addition, the dynamical behavior is perturbed by the complex distribution of local fields, inducing frustration in the mobility of the individual moments and partially suppressing the superparamagnetic magnetic relaxation.[40] Magnetic frustration has been observed in assemblies of nanoparticles embedded in dextran or starch coatings[41] or for cell-internalized nanoparticles which strongly interact with each other within intracellular compartments.[42] An example of such behavior is given by commercial particles (BNF−starch, Micromod Partikeltechnologie, GmbH), which consists of multiple 15−20 nm magnetite crystals that form fractal aggregates (85−90 wt %) in a hydroxyethyl starch shell (d_{HYD} = 107 nm; see magnetic characterization in Supporting Information, Figure S6). This material shows reduced magnetization (Figure S6), which saturated at much larger fields (2000 kA/m) than for nanoflowers and lower saturation magnetization (M_s = 59.1 $A \cdot m^2 \cdot kg^{-1}$). The decrease of reduced remanence at 5 K (M_r/M_s = 0.26) provides further evidence of the disordering effect of dipolar interactions.[43] Similarly, polycrystalline hollow maghemite spheres are characterized by enhanced anisotropy, magnetic frustration, and diminished magnetization compared to the plain nanoparticles, with these features being ascribed to the multiple crystallographic domains of the shell, which are randomly oriented and thus present different anisotropy axes, and to the high number of pinned spins at the shell surface and crystallite interfaces, which increase surface disorder and apparent anisotropy.[44] A physical situation opposite to that described above results in the opposite effects in the case of our multi-core nanoparticles.

Indeed, the enhanced magnetization of multi-core nanoparticles rules out the possibility of a disordered organization of magnetic cores coupled through dipole−dipole interactions alone, which would induce a decrease in effective magnetization. We therefore hypothesize the presence of exchange interactions between surface atoms of neighboring cores. Exchange interactions between particles with different orientation of their easy axes can indeed result in a rotation of the spin structure, as first observed for nanoparticles of hematite which were in direct physical contact.[45] Due to the synthetic procedure we have adopted, the magnetic cores are in sufficiently close proximity that their crystallographic orientation continues across the interface. The enhancement of their magnetization per unit of mass, evidenced in Figure 4B, could result from collective behavior of spins at the interface, due to exchange interactions. Moreover, we can interpret the observed reduction of magnetic anisotropy as a consequence of magnetic ordering at the grain's interface. Discontinuity of exchange interactions at particle surfaces can perturb the ferromagnetic order, resulting in surface spin disorder, as evidenced by different techniques.[46,47] In the case of nanoflowers, the overall surface anisotropy is reduced on coalescence of individual cores because magnetic continuity is at least partially restored at the core interfaces. Ferromagnetic resonance (FMR) also confirms the distinct magnetic behavior of the multi-core structures. A single broad resonance line is observed for single cores, and we attribute the broadening to the wide distribution of internal fields arising from surface spin disorder as previously observed.[48,49] In contrast, multi-core particles show a complex resonance spectrum, consisting of several absorption lines at different resonance fields, which are lower than the resonance field of single cores (Figure 4F). The additional exchange interactions occurring at the grain boundaries could account for the high local fields experienced by electronic spins and explain the highly asymmetrical appearance of the FMR spectrum.

Hyperthermia Performance Is Enhanced by Cooperative Behavior. In an attempt to correlate the magnetic and structural properties reported above with the hyperthermia performance of multi-core nanostructures, we measured SAR values over a wide range of magnetic field amplitudes and frequencies. Under all conditions, we observed a 2−10-fold SAR increase for multi-core with respect to single-core materials. The best SAR was obtained for the one-pot synthesis with a stoichiometric mixture of polyol solvent (MC0). Under field conditions of 29 kA/m and 520 kHz, the temperature increased at a rate of 1.04 °C/s for an iron concentration of 0.087 M *versus* 0.15 °C/s (0.081 mM) for SC nanoparticles (Figure 5A, Supporting Information, Figure S7). Among the size-sorted multi-core samples, the largest sized nanoparticles produced the highest SAR (Figure 5B). The heating performance of these multi-core nanoparticles is much higher than those

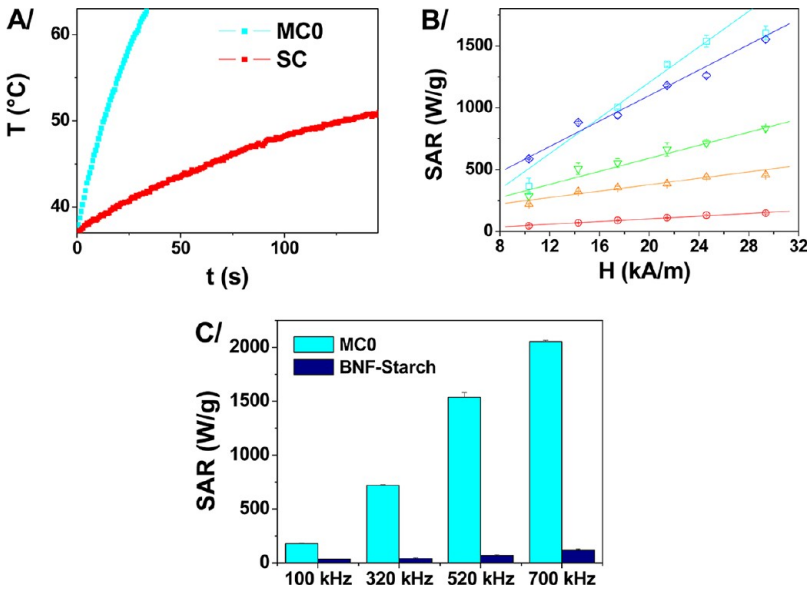

Figure 5. Magnetothermal properties for the different samples. (A) Heating curve for MC0 and SC samples at a concentration of 0.087 and 0.081 mM in iron, respectively. Temperature was recorded every 0.7 s under an alternative magnetic field $H = 29$ kA/m and at frequency $f = 520$ kHz. (B) SAR values as a function of the applied magnetic field at frequency $f = 520$ kHz for MC0 (cyan), MC1 (blue), MC2 (green), MC3 (orange), and SC (red). (C) SAR value comparison between MC0 and BNF−starch at different frequencies for a magnetic field $\mu_0 H = 25$ kA/m.

reported for spherical single-core maghemite nanoparticles.[13,14,50] In fact, they lie among the best performing materials reported so far for iron oxide, including maghemite nanocubes[17,19] and bacterial magnetosomes.[51] It is worth noting that we did not observe the dependence on the square of the magnetic field amplitude that is predicted by the linear theory for non-interacting superparamagnetic nanoparticles.[11] Similarly, the field strength threshold predicted by the Stoner−Wohlfarth model,[52] and reported experimentally for metallic iron nanocubes,[53] was not observed in our experiments. Instead, the SAR increased proportionally to the field strength (Figure 5B) and frequency (Figure 5C), a behavior that is not anticipated by the current models.

It is particularly instructive to compare our structures to BNF−starch nanoclusters described above, which have been reported as the best multi-core candidates for hyperthermia due a strong increase of their SAR at high field.[54] Irrespective of the field strength used, we found SAR values for BNF−starch that were 20 times lower than that of our cooperative MC nanoparticles (Figure 5C). Multi-core clusters prepared by co-precipitation and embedded into a carboxymethyldextran shell also showed lower heating performance.[41] These comparisons emphasize the crucial role that different magnetic interactions may have on heating mechanisms.[55] Specifically, theoretical investigations have shown the detrimental effect of dipole−dipole interparticle interactions on heating efficiency.[56,57] Focusing on intercore dipolar interactions taking place in a dense three-dimensional cluster of nanoparticles, a reduced hysteresis area was found in comparison to non-interacting nanoparticles. Although complex dynamical effects must be explicitly considered when simulating the high frequency response of nanoparticles, the main effect of dipolar interactions is a demagnetization process leading to a decrease in susceptibility and hysteresis losses.[40,57] In contrast, for multi-core nanoparticles, we clearly observed enhancement of heating performance, which arises from clustering, coalescence, and magnetic reorganization of elementary magnetic grains during the preparation. In agreement with the findings from the magnetic and structural characterization, the hyperthermic performance further confirms that dipole−dipole interactions are not the main determinant of hysteresis losses in our materials. On the contrary, the latter findings highlight the role of magnetic ordering and exchange interactions at the grain interfaces; a combination of reduced anisotropy and enhanced magnetic moment preserves the superparamagnetic-like behavior of the multi-core nanoparticles and simultaneously potentiates thermal losses. Although the observed behavior is beyond the predictive capabilities of current models, tuning particle architecture to favor cooperative magnetic behavior has been established for the first time as an alternative strategy to enhance heating efficiency.

To confirm the biological value of citrate-coated multi-core nanoparticles for cancer treatment, their interactions with the human breast cancer MCF-7 cell line were investigated. Cells were incubated with the best performing sample (MC0) at different iron concentration, ranging from 0.2 to 5 mM in serum-free

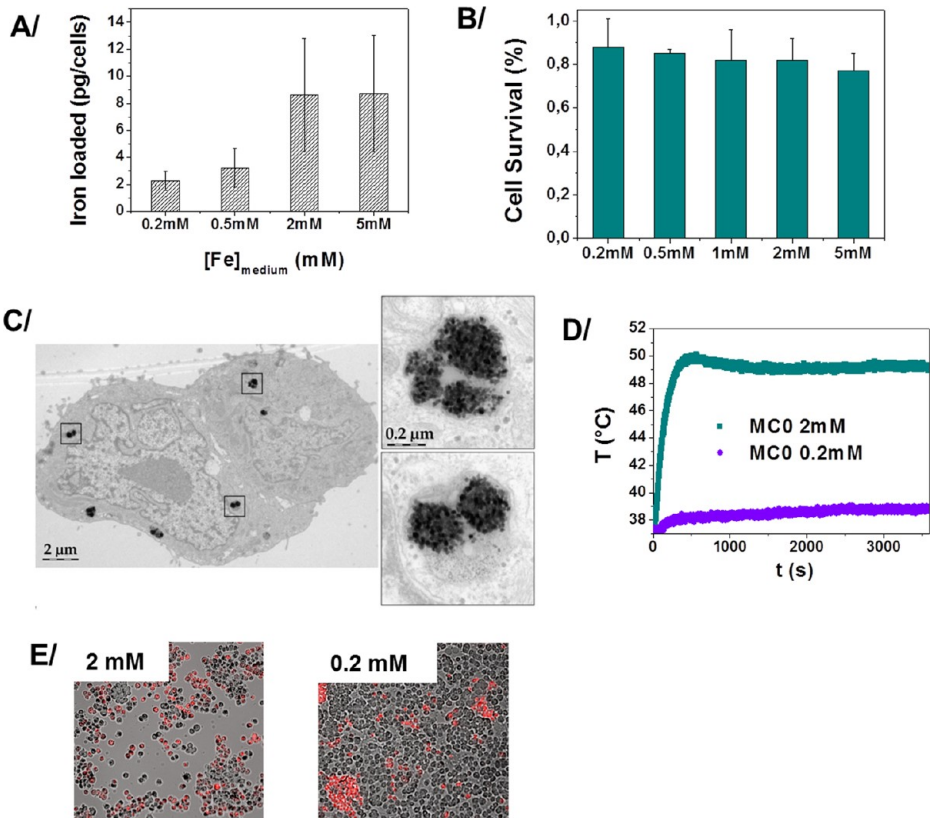

Figure 6. *In vitro* **evaluation of MCF-7 tumor cells after incubation with MC0 suspension for 30 min. (A) Average uptake of iron per cell (in pg) determined by magnetophoresis analysis after incubation with MC0 at different iron concentrations for 30 min. Bars represent the width of the distribution of iron load in the cell population. (B) Cell metabolic activity assayed by Alamar Blue test and expressed as percentage of the value for control nonlabeled cells. All points have been acquired in triplicate. (C) TEM micrographs of MCF-7 cells after labeling with MC0 at an iron concentration of 2 mM. Nanoflowers are confined into intracellular lysosomes. (D,E) Therapeutic efficacy of MC0 nanoparticles internalized in MCF-7 tumor cells. (D) Temperature increase in a pellet of 300 μL containing 2×10^6 MCF-7 labeled cell during exposure to an alternative magnetic field of 29 kA/m at frequency of 520 kHz. MCF-7 cells were previously labeled with 0.2 or 2 mM iron concentration for 30 min. (E) Cell death assessment using propidium iodide assay after 1 h exposure to the alternative magnetic field. Dead cells appear as red fluorescence.**

RPMI culture medium. Following 30 min incubation at 37 °C, the cells were washed and trypsinized to assess their nanoparticle uptake by single-cell magnetophoresis, as described elsewhere.[58] Cell mobility toward a calibrated magnet was measured for 200 cells, yielding the whole distribution of magnetic load per cell. We did not observed any aggregation of nanoparticles onto cells. As seen in Figure 6A, cell uptake was dose-dependent and saturated for extracellular iron concentration of 2 mM to an average iron load of 8 pg/cell. The metabolic activity of the labeled cells assessed by Alamar Blue test was not significantly modified compared to the control (Figure 6B). Electron microscopy confirms the intracellular uptake of nanoparticles which were confined into cell endosomes or lysosomes (Figure 6C). As demonstrated previously for nanoparticles synthesized by co-precipitation,[59,60] the citrate ligands enable facile adsorption of nanoparticles on the cell plasma membrane, which triggers rapid and efficient uptake by tumor cells through endocytosis. In contrast, much longer time would be needed to achieve similar uptake with dextran- or polymer-coated nanoparticles due to the poor affinity to the cell membrane.[61] This can represent a decisive advantage for cancer treatment since it ensures the biopersistance of nanoparticles in the tumor and favors intracellular distribution. Therapeutic efficacy was tested on tumor-mimicking pellets (300 μL) containing 10^6 MCF-7 cells, previously incubated for 30 min with 0.2 or 2 mM iron concentration. Iron content in the cell pellet was quantified to be 2×10^{-5} and 2.8×10^{-4} g, respectively. The agreement of global iron dosage (by elemental analysis) and single-cell iron load, as well as transmission electron microscopy, confirmed that all nanoparticles were intracellular. Upon exposure to an oscillating magnetic field of 520 kHz and 29 kA/m, the pellet was heated to a plateau temperature of 39 °C for the lower and 49 °C for the higher Fe concentration (Figure 6D). Twenty percent of cells became necrotic after 1 h of treatment for the lower, as opposed to 60% for the higher concentration condition. Thus, the dose-dependent thermal effect directly translates to a dose-dependent cytotoxicity under field exposure (Figure 6E). It should be

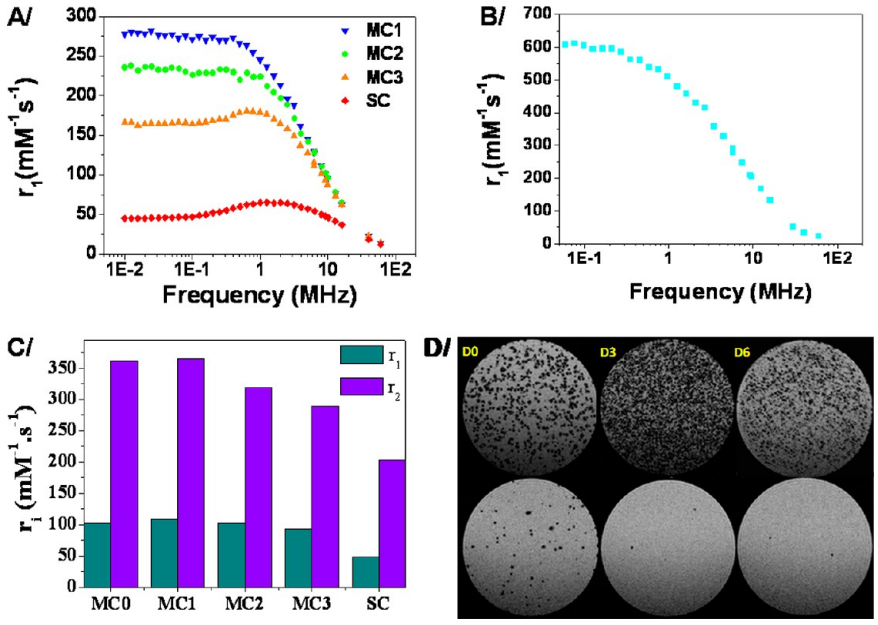

Figure 7. ^{1}H NMR result for the different samples. Longitudinal relaxivity (r_1) presented through their NMR-D profile (A) for size-sorted nanoparticle synthesis from a nonstoichiometric polyol mixture (SC and MC1−3) and (B) for a stoichiometric mixture (MC0). (C) Comparison of the longitudinal (r_1) and transverse (r_2) relaxivities for the different samples at 9.25 MHz. (D) High-resolution 4.7 T MR images of agarose gels containing dispersed MCF-7 cells (5×10^4 cells/mL) labeled with MC0 (top line) or BNF−starch (bottom line) (2 mM iron concentration for 30 min) at day 0, day 3, and day 6 postlabeling. Represented slice thickness is 2 mm, and in-plane resolution is 50 μm × 50 μm.

noted that the iron dose per milliliter of cell culture in this study was 10−100-fold lower than the total dose injected in the tumor in murine or human hyperthermia assays.[1,17,18]

Nuclear Magnetic Resonance Performance Is Enhanced by Cooperative Magnetic Behavior. To characterize multi-core nanoparticles as theranostic agents, the next step was to evaluate their efficacy as MRI contrast agents. By producing local magnetic fields experienced by water molecules, superparamagnetic nanoparticles accelerate the relaxation of the ^{1}H magnetization. The spin−lattice (r_1) and spin−spin (r_2) relaxivities are defined as concentration-independent measures of the relaxation rate enhancement for the longitudinal and transverse components of the magnetization, respectively. A combined optimization of both r_1 and r_2 is required to improve detection sensitivity in MR sensing and imaging, with the specific requirements depending on the selected imaging modality. However, r_1 and r_2 relaxivities are highly sensitive, but in a quite different way, to some intrinsic properties of nanoparticles such as their size, magnetization, and dynamics of the magnetic moment, as well as extrinsic factors such as their spatial distribution, clustering, or organization in the carrier medium. Detailed investigation of the longitudinal relaxation properties can be obtained from nuclear magnetic resonance dispersion (NMRD), which provides r_1 measurements over a wide range of ^{1}H resonance frequency (0.01 to 20 MHz) or equivalently of magnetic field strength (0.25 mT to 0.5 T).[62]

We can observe in Figure 7A that the NMRD profile was dramatically modified for multi-core with respect to single-core nanoparticles. The 10 nm SC suspension displays a profile which is characteristic of superparamagnetic nanoparticles and is well predicted by the seminal model based on outer sphere theory and includes a Curie component to the relaxation.[12] The presence of a maximum (whose position depends on particle size and anisotropy) is interpreted as the consequence of Néel fluctuations of the particle's magnetic moment. In strong contrast, multi-core nanoparticles show a monotonous decrease of relaxivity with increasing frequency. For size-sorted MC, the low-field relaxivity is enhanced and the maximum progressively disappears when the size of multi-core nanoparticles is increased. Moreover, it is particularly unexpected to observe such high values of low field relaxivity, which culminate at around 600 mM^{-1} s^{-1} for the MC0 sample (Figure 7B). NMRD profiles with similar shape were previously observed for clustered materials formed from core−shell iron−iron oxide nanoparticles,[63] or by linking an iron oxide nanoparticle by DNA strands[64] or with fatty acids,[65] but with significantly lower low-frequency relaxivity than is reported here. In all of these cases, the hydrodynamic size was far larger than for nanoflowers.

A model for the effect on r_1 of the formation of aggregates, for which the water residence times within the nanostructure are extended, has been developed and experimentally validated.[66] The NMRD

profiles were more and more flattened on increasing agglomeration. It could be argued that such effects could play a role in the unusual relaxivity of the aggregated NP suspensions noted above.[63−65] On the contrary, the huge relaxivity enhancement exhibited by dispersed multi-core nanoparticles arises due to their intrinsic magnetic properties. On the basis of recent theoretical modeling (Levy *et al.*, unpublished), we hypothesize that the increased low-field r_1 arises from slowing of the dynamics of the magnetic moments (*i.e.*, progressive blocking of Néel fluctuations due to the local magnetocrystalline field). This assumption is fully consistent with the shift of blocking temperature observed in ZFC magnetization curve. Hence the unprecedented low-frequency r_1 values of multi-core nanoparticles makes them particularly useful as T_1 contrast agents for MR-based sensing and for the growing field of micro-Tesla MRI.[67]

Regarding their potency as T_2 agents for clinical MRI, the multi-core nanoparticles exhibit remarkably high values of r_2 (Figure 7C). The r_2 increased by a factor of 1.8 for multi-core with respect to single-core nanoparticles and also increased with size for the former, as is generally expected in this size range.[68] The maximum observed was 365 s^{-1} mM^{-1} (at 9.25 MHz) for multi-core particles of d_{HYD} = 39 nm. Enhanced r_2 values have been recently demonstrated for multiple particles encapsulated in a substrate matrix. The r_2 values of 300−500 s^{-1} mM^{-1} have been reported for hydrogel-stabilized nanoparticle clusters.[69] The effect of core and cluster size has been studied for block-copolymer-stabilized clusters, with r_2 maxima in the range of 200−400 s^{-1} mM^{-1} found for clusters of size ranging from 80 to 120 nm, depending on the core size.[68] This type of behavior can be explained using outer sphere theory taking into account the large magnetic moment of the assembly and the volume fraction of magnetic material.[68,70] In these and all related cases, the hydrodynamic size was significantly in excess of 50 nm, a factor that can significantly affect blood circulation time for real applications.

Our multi-core constructs present several advantages as compared to encapsulated nanoparticles; the absence of a matrix and resulting close contact of the individual cores gives rise to cooperative behavior which amplifies the global magnetic moment, while maintaining the hydrodynamic size below 40 nm and retaining superparamagnetic properties and remarkable colloidal stability. As a result, the r_2 values are significantly higher than has been reported (range 33−67 s^{-1} mM^{-1}) for dispersed single domain spherical nanoparticles.[71,72] Recently, r_2 values in excess of 700 s^{-1} mM^{-1}, which is close to the theoretical maximum, have been reported for PEG-phospholipid-stabilized iron oxide nanocubes.[73] Taken together, that study[73] along with this work demonstrates that, once nanoparticle dispersion is sufficiently good, long-circulating high r_2 agents may be realized. In addition to the new insights gained into collective magnetic behavior, the additional advantages of the multi-core nanoflower suspensions presented here are that collective effects modify the dynamics of the magnetic moment in such a way that *both* the longitudinal and transverse relaxivities are enhanced, while the citrate coating provides specific advantages for cell labeling.

Finally, to confirm the potency of multi-core nanoparticles for high-field MRI, as well, tumor cells labeled with MC0 and dispersed in agarose gel were imaged using a high-resolution cryoprobe adapted on a 4.7 T scanner. Cell detection was monitored over 6 days after labeling, during which time the cells underwent approximately six divisions. For comparison, we imaged the same cells labeled with BNF−starch particles under the same conditions. As shown in Figure 7D, the cells could be detected individually when labeled with MC0, but only a few cells were depicted on labeling with BNF−starch. Remarkably, single-cell depiction was still possible after 6 days of cell division of MC0-labeled tumor cells, although the contrast was somewhat diminished. These findings demonstrate the tremendous potential of multi-core cooperative nanoparticles for cell imaging by MRI.

CONCLUSION

We have demonstrated that highly crystalline multi-core iron oxide nanoparticles synthesized by a polyol process display collective magnetic behavior that potentiates their magnetic properties in comparison to single-core counterparts. By applying electrostatic colloidal sorting, we demonstrated modulation of the size and magnetic interactions in the materials. The close contact between cores within the particles ensures a continuity of the crystalline orientation and favors magnetic ordering across the interfaces. The resulting magnetically cooperative multi-core nanoparticles, of about 25 nm in diameter, retain superparamagnetic properties at room temperature with optimized magnetic dynamics. As a result, the materials show enhanced longitudinal and transverse relaxivities for MRI contrast generation and enhanced SAR values for magnetic hyperthermia. In contrast to matrix-embedded clusters, in which the emergent magnetic behavior is dominated by dipole−dipole interactions, we clarify for the first time the critical role of exchange coupling within multi-core nanostructures in affording improved magnetic properties for multiple applications. In addition, citrate-coated iron oxide nanostructures are nontoxic, highly stable in biological media, and easily internalized in tumor cells, allowing for their MRI detection after several cell divisions and destruction by magnetic hyperthermia. By investigating the role of nanoparticle

architecture in modulating magnetic properties, this study pinpoints new strategies to improve therapeutic and diagnostic effectiveness of biocompatible nanostructures.

EXPERIMENTAL SECTION

Chemicals. The syntheses were carried out using commercially available reagents. Iron(II) chloride hexahydrate ($FeCl_2 \cdot 4H_2O$ 99%), iron(III) nitrate nonahydrate ($Fe(NO_3)_3 \cdot 9H_2O$ 98%), sodium hydroxide (NaOH, 99.99%), diethylene glycol (DEG, 99%), *N*-methyldiethanolamine (NMDEA, 99%), sodium citrate tribasic dihydrate (98%), and nitric acid (HNO_3, 70%) were purchased from Sigma-Aldrich (France). Iron(II) chloride tetrahydrate ($FeCl_3 \cdot 6H_2O$ 99%), ethanol, acetone, and ethyl acetate were obtained from VWR (France).

Nanoparticle Synthesis. First, 1.082 g (4 mmol) of $FeCl_3 \cdot 6H_2O$ and 0.398 g (2 mmol) $FeCl_2 \cdot 4H_2O$ were completely dissolved in 80 g of liquid mixture of NMDEA and DEG with 1:1 (v/v) ratio. The solution was stirred for 1 h. Separately, 0.64 g (16 mmol) of NaOH was dissolved in 40 g of polyols. This solution was added to the solution of iron chlorides, and the resulting mixture was stirred for another 3 h. Then, the temperature was elevated to 220 °C using a progressive heating of 2 °C/min. Once the temperature reached 220 °C, the solution was stirred for 12 h. The black sediments were separated magnetically and washed with mixture of ethanol and ethyl acetate (1:1, v/v) several times to eliminate organic and inorganic impurities. Possible iron hydroxides were removed by treatment with 10% nitric acid. Then, 8.25 g of iron(III) nitrate was then dissolved in 20 mL water and added to the nanoparticles. The resulting mixture was heated to 80 °C for 45 min to achieve a complete oxidation of the nanoparticles. After another treatment with 10% nitric acid, the particles were washed twice with acetone and diethyl ether and dispersed in water, and MC0 nanoparticles were obtained.

With the same procedure but using a polyol mixture of NMDEA and DEG with 0.66/0.33 (v/v) ratio and a heating time at 220 °C equal to 4 h, a stable suspension of polydisperse nanoparticles in water was obtained. The concentration of the sample was approximately 1.2 mol/L of iron; 250 mL of concentrated nitric acid was added to 10 mL of the nanoparticle suspension. Two phases appeared instantaneously: a phase concentrated in nanoparticles (the flocculate) at the bottom of the vial, and a more diluted one containing the smaller nanoparticles (the supernatant). After 5 min of magnetic decantation to ensure a rapid phase separation, the supernatant was pipetted into another vial. Seven milliliters of water was added to the flocculate to allow a full dispersion of the nanoparticles in this phase. Further size sorting steps were then experienced on the two phases to ensure a low polydispersity of the samples. Among the different fraction obtain, four fractions were used for the study: MC1, MC2, MC3, and SC (see Supporting Information S1).

The iron content of each sample was titrated using flame atomic absorption spectroscopy. To ensure a good colloidal stability at physiological pH, citrates anions were adsorbed at the nanoparticle surface with a citrate to iron molar ratio of 0.2. This functionalization was performed for all samples (MC0, MC1, MC2, MC3, and SC).

Nanoparticle Characterization. *Aberration-Corrected HRTEM and Electron Tomography.* The newly developed JEOL ARM200F electron microscope, equipped together with a CEOS aberration corrector and a cold-field emission gun,[74,75] was used for high-resolution imaging and tomography experiments. The tomography data set consisting of 216 bright-field images was collected between +73° and −73° using the Saxton scheme, where the tilt increment depends on the cosine of the overall tilt angle. After a fine alignment of all projections, the volume reconstruction was calculated using the simultaneous iterative reconstruction technique (SIRT) with 10 iterations.[76] Volume rendering and slices of the tomogram were generated using the Amira module included in the tomography package of the digital micrograph software (Gatan).

Dynamic Light Scattering. Stability of the colloidal suspension of citrate nanoparticles was investigated using a Zeta Sizer (Malvern Instruments) equipped with a 4.0 mW He−Ne laser operating at 633 nm and an Avalanche photodiode detector. The same apparatus was used for zeta-potential measurement. Stability of the samples was measured on suspension containing 5 mM of free citrate ions and a total iron concentration of 10^{-2} mol/L.

Specific Surface Area Determination. For the specific surface area measurements, the samples were lyophilized 24 h and then degassed overnight at 110 °C under vacuum (10^{-6} bar). Volumetric adsorption of nitrogen at 77 K was performed on a ASAP 2020 Micromeretics apparatus. The specific surface area was measured using the BET equation on the isotherm between $P/P_0 = 0-0.2$.

X-ray Diffraction. The crystalline structure of the samples was identified by X-ray diffraction (XRD). X-ray diffractograms were collected at room temperature using a D500 Siemens diffractometer equipped with a quartz monochromator.

Magnetic Characterization. Magnetization measurements were collected with a Quantum Design MPMS-5S SQUID magnetometer working in the temperature range of 1.8−350 K and the magnetic field range of 0−3980 kA/m. All magnetic measurements were performed in solutions around 10 mM in [Fe]. Data were corrected for the diamagnetic contribution.

Ferromagnetic resonance (FMR) spectra were obtained using a Varian ESR spectrometer operating at 9.26 GHz (X band) with the following parameters: microwave power = 1 mW, modulation frequency = 100 kHz, modulation field = 10 G. FMR spectra were recorded at room temperature for 2 μL of nanoparticle suspension at a concentration of 10 mM.

Hyperthermia Measurement. The evaluation of heat generation was performed with a home-built magnetothermal setup.[13] It consists of a resonant RLC circuit with a 16 mm coil. The field amplitude can be varied from 5 to 29 $kA \cdot m^{-1}$ and the magnetic field frequency from 320 kHz to 1.1 MHz. Then, 300 μL of a solution of magnetic NPs was put inside the coil, and the temperature was probed with a fluoro-optic fiber thermometer (Luxtron Corp., CA) every 0.7 s. By circulating nonane into the coil, the temperature inside the sample holder was kept to 37 °C. Although the system is optimized for working in adiabatic conditions, temperature dissipation with the surrounding air was observed.

The SLP was calculated using the following formula:

$$\mathrm{SAR} = \frac{1}{m_e}\left(\sum_i c_i m_i \frac{dT}{dt}\right)$$

where m_e is the total mass of the iron, c_i is the specific heat, and m_i is the weight of the different species in solution; finally, dT/dt is the slope of the $T(t)$ curve. Because the experimental setup we used is not perfectly adiabatic, the dT/dt value was extrapolated by taking the initial slope of temperature increase obtained from the linear term of a polynomial fit of the whole curve. The mass of iron is measured by flame atomic absorption spectroscopy. The iron concentration was 87 mM for MC0, 54 mM for MC1, 12 mM for MC2, 9 mM for MC3, 81 mM for SC, and 100 mM for BNF−starch.

NMRD and Relaxivity Measurements. The frequency dependence of the ^{1}H relaxation for the aqueous nanoparticle suspensions was recorded over the frequency range of 0.01−20 MHz using a Spinmaster FFC-2000 fast-field cycling NMR relaxometer (Stelar SRL, Mede, Italy). The system operated at a measurement frequency of 9.25 MHz for ^{1}H, where the 90° pulse was 7 μs. T_1 measurements were performed as a function of external field, B_0, with standard pulse sequences incorporating B_0 field excursions. The temperature of the samples was maintained at 25 ± 1 °C using a thermostatted airflow system. All of the ^{1}H

magnetization recovery curves were singly exponential within experimental error, and the random errors in fitting T_1 were always less than 1%. T_2 was measured using the CPMG pulse sequence.

Cell Labeling and Uptake Assay. Dulbecco's modified Eagle eedium (DMEM), Roswell Park Memorial Institute medium (RPMI-1640 medium), trypsin solution, and all other reagents used for cell culture were purchased from PAA and used with no further purification. MCF-7 cells (ATCC #HTB-22) were maintained as monolayer cultures in DMEM supplemented with 10% fetal bovine serum (FBS), 1% penicillin-streptomycin at 37 °C, and 5% of CO_2. The incubation medium was prepared by adding a filter-sterilized suspension of nanoparticles with different iron concentration dispersed in serum-free RPMI-1640 medium supplemented with 5 mM of citrate. Cells were incubated with this medium for 30 min at 37 °C. After three rinsing steps with RPMI medium, cells were trypsinized, centrifuged at 1200 rpm for 5 min, and rinsed again two times with RPMI. Subsequently, the total iron concentration in cell pellets (containing a known number of cells) was quantified by flame atomic absorption spectroscopy. To bring a more specific measurements of cell iron load, single-cell magnetophoresis assay was used as described before.[58] Briefly, the cell magnetic load was quantified by measuring the velocity of magnetically labeled cells in suspension when they are submitted to a magnetic field gradient. In the steady state regime, the magnetic driving force acting on cells is defined as $F_m = N \times \mu \times \text{grad}B$, where N is the number of cell-associated NPs, μ the NP magnetization in the applied magnetic field B = 150 mT, and grad$B$ = 17 T/m, the magnetic field gradient. This force is counterbalanced by the viscous force $F_V = 3\pi \times \eta \times d_{cells} \times v_{cells}$, where d_{cells} is the cell diameter (cells in suspension are assimilated to spheres), v_{cells} is the cell velocity, and η is the viscosity of the carrier fluid. The cell magnetic moment (or equivalently the iron mass per cell) is thus derived from the measured cell velocity and cell diameter. The magnetophoretic movement of cells toward the magnet was recorded by videomicroscopy. For each condition of incubation, the velocity and diameter of about 200 cells were measured, yielding the distribution of iron load in the cell population. Iron load per cell was expressed as a mean ± (standard deviation for three independent experiments).

Cell Viability Test. In order to evaluate the toxicity of MC0 nanoparticles on cells, their metabolic activity was assessed by the Alamar Blue test. One thousand cells were seeded in 48-well plates and submitted to the labeling procedure the day after. MCF-7 cells were incubated for 30 min at 37 °C with MC0 nanoparticles dispersed in RPMI-1640 (supplemented with 5 mM sodium citrate) at different iron concentration from 0.2 to 5 mM. The labeled MCF-7 cells were then washed twice in PBS and were incubated with 10% Alamar Blue in culture medium for 2 h. The fluorescence in cell medium due to the reduction of resazurin (oxidized form) to resorufin by cell activity was quantified on a FLUOstar OPTIMA microplate reader (excitation 550 nm, emission 590 nm) and compared to the control nonlabeled cells. The conditions were run in quadruplicate.

Hyperthermia Performed in Cells. MCF-7 cells were grown up to a confluent state in a 75 cm^2 culture flask. The culture medium was replaced with 6 mL of MC0 nanoparticles dispersed in RPMI-1640 (supplemented with 5 mM sodium citrate) at an iron concentration [Fe] = 2 or 0.2 mM and labeled for 30 min with the procedure described above. After rinsing steps and trypsination, cells were centrifuged and the cell pellet was transferred in a sample vial, yielding a cellular suspension of 2×10^6 MCF-7 cell in 300 μL of PBS. The cells were finally tested in a hyperthermia setup, by applying an alternating magnetic field at a frequency of 520 kHz and at magnetic field amplitude of 29 kA·m^{-1} for 1 h. The cell death was evaluated using propidium iodide salt (PI). The PI is commonly used for identifying dead cells in a population. PI salt was purchased from Sigma-Aldrich (95%) and used without further purification. After hyperthermia application, 10 μL of PI was added to cells and left for about 10 min at room temperature. Then cells were carried up on slide and coverslip and observed using an inverse microscope (Leica DM IRB, Solms, Germany) coupled to a high sensitive CCD camera (CoolSNAP, Photometrics, Tucson, Arizona). A large number of cells (around 4000) were counted using Image J software to determine the rate of dead cells after hyperthermia application.

High-Resolution MRI. MRI was performed using a 4.7 T preclinical MRI system (BioSpec 47/40 USR, Bruker) in the Small Animal Imaging Platform Paris–Descartes PARCC-HEGP. High-resolution MRI was carried out using a cryogenic probe (CryoProbe, Bruker) in 0.3% low-melting-point agarose gels where labeled cells were dispersed at a density of 5×10^4 cells/mL. Scans were run under a fast steady state precession (FISP) protocol on FID mode. Images were acquired using a T_2*-weighted sequence with following parameters: FOV of 9 × 9 × 9 mm; matrix of 180 × 180; voxel size of 50 × 50 × 50 μm; echo time of 5 ms, repetition time of 20 ms; flip angle of 25°, and bandwidth SW of 50 kHz.

Transmission Electron Microscopy in Cells. Ultrathin sections (80 nm) of MCF-7 cells labeled with MC0 were stained by lead citrate and were examined by using a ZEISS EM902 TEM operated at 80 kV (Carl Zeiss-France, MIMA2Microscopy Platform, UR1196, INRA, Jouy en Josas, France). Images were acquired with a charge-coupled device camera (Megaview III) and analyzed with ITEM Software (Eloïse, France). Beforehand, cells were washed three times in 0.1 M cacodylate buffer and fixed with 2.5% glutaraldehyde in cacodylate buffer at 4 °C for 30 min. Cells were postfixed with osmium tetraoxide 1% and passed through uranyl acetate. Samples were then dehydrated in an ethanol series (30–100%) and embedded in epoxy medium (EPON 812; Shell Chemical, San Francisco, California).

Conflict of Interest: The authors declare no competing financial interest.

Acknowledgment. The authors thank J. Servais for technical assistance in hyperthermia measurements, F. Gendron for SQUID and FMR experiments, E. Briot for the nitrogen adsorption isotherms, C. Péchoux and S. Chat for electron microscopy, G. Autret, O. Clément, and J. Kolosnjaj for MRI experiments and image processing, and F. Carn (MSC) for light scattering experiments. This work was supported by the Region Ile-de-France (convention SESAME E1845 for the JEOL ARM 200F electron microscope recently installed at the Paris Diderot University and PhD grant for P.H.) and by the European project Magnifyco (Contract NMP4-SL-2009-228622).

Supporting Information Available: Figures illustrating experimental procedure, giving further characterizations, including high-resolution TEM, XRD spectra, BET measurements, and magnetothermal measurements, and theoretical appendix for the ZFC/FC fit are provided as Supporting Information. This material is available free of charge *via* the Internet at http://pubs.acs.org.

REFERENCES AND NOTES

1. Maier-Hauff, K.; Ulrich, F.; Nestler, D.; Niehoff, H.; Wust, P.; Thiesen, B.; Orawa, H.; Budach, V.; Jordan, A. Efficacy and Safety of Intratumoral Thermotherapy Using Magnetic Iron-Oxide Nanoparticles Combined with External Beam Radiotherapy on Patients with Recurrent Glioblastoma Multiforme. *J. Neuro-Oncol.* **2011**, *103*, 317–324.
2. Amstad, E.; Kohlbrecher, J.; Muller, E.; Schweizer, T.; Textor, M.; Reimhult, E. Triggered Release from Liposomes through Magnetic Actuation of Iron Oxide Nanoparticle Containing Membranes. *Nano Lett.* **2011**, *11*, 1664–1670.
3. Stanley, S. A.; Gagner, J. E.; Damanpour, S.; Yoshida, M.; Dordick, J. S.; Friedman, J. M. Radio-Wave Heating of Iron Oxide Nanoparticles Can Regulate Plasma Glucose in Mice. *Science* **2012**, *336*, 604–608.
4. Yoo, D.; Lee, J.-H.; Shin, T.-H.; Cheon, J. Theranostic Magnetic Nanoparticles. *Acc. Chem. Res.* **2011**, *44*, 863–874.
5. Kievit, F. M.; Zhang, M. Surface Engineering of Iron Oxide Nanoparticles for Targeted Cancer Therapy. *Acc. Chem. Res.* **2011**, *44*, 853–862.
6. Tassa, C.; Shaw, S. Y.; Weissleder, R. Dextran-Coated Iron Oxide Nanoparticles: A Versatile Platform for Targeted

Molecular Imaging, Molecular Diagnostics, and Therapy. *Acc. Chem. Res.* **2011**, *44*, 842–852.
7. Lee, J. E.; Lee, N.; Kim, T.; Kim, J.; Hyeon, T. Multifunctional Mesoporous Silica Nanocomposite Nanoparticles for Theranostic Applications. *Acc. Chem. Res.* **2011**, *44*, 893–902.
8. Ho, D.; Sun, X.; Sun, S. Monodisperse Magnetic Nanoparticles for Theranostic Applications. *Acc. Chem. Res.* **2011**, *44*, 875–882.
9. Lee, J.-H.; Jang, J.-t.; Choi, J.-s.; Moon, S. H.; Noh, S.-h.; Kim, J.-w.; Kim, J.-G.; Kim, I.-S.; Park, K. I.; Cheon, J. Exchange-Coupled Magnetic Nanoparticles for Efficient Heat Induction. *Nat. Nanotechnol.* **2011**, *6*, 418–422.
10. Jang, J.-t.; Nah, H.; Lee, J.-H.; Moon, S. H.; Kim, M. G.; Cheon, J. Critical Enhancements of MRI Contrast and Hyperthermic Effects by Dopant-Controlled Magnetic Nanoparticles. *Angew. Chem., Int. Ed.* **2009**, *48*, 1234–1238.
11. Rosensweig, R. E. Heating Magnetic Fluid with Alternating Magnetic Field. *J. Magn. Magn. Mater.* **2002**, *252*, 370–374.
12. Roch, A.; Muller, R. N.; Gillis, P. Theory of Proton Relaxation Induced by Superparamagnetic Particles. *J. Chem. Phys.* **1999**, *110*, 5403–5411.
13. Fortin, J. P.; Wilhelm, C.; Servais, J.; Menager, C.; Bacri, J. C.; Gazeau, F. Size-Sorted Anionic Iron Oxide Nanomagnets as Colloidal Mediators for Magnetic Hyperthermia. *J. Am. Chem. Soc.* **2007**, *129*, 2628–2635.
14. Lartigue, L.; Innocenti, C.; Kalaivani, T.; Awwad, A.; Sanchez Duque, M. d. M.; Guari, Y.; Larionova, J.; Guérin, C.; Montero, J.-L. G.; Barragan-Montero, V.; *et al.* Water-Dispersible Sugar-Coated Iron Oxide Nanoparticles. An Evaluation of Their Relaxometric and Magnetic Hyperthermia Properties. *J. Am. Chem. Soc.* **2011**, *133*, 10459–10472.
15. Levy, M.; Luciani, N.; Alloyeau, D.; Elgrabli, D.; Deveaux, V.; Pechoux, C.; Chat, S.; Wang, G.; Vats, N.; Gendron, F.; *et al.* Long Term *In Vivo* Biotransformation of Iron Oxide Nanoparticles. *Biomaterials* **2011**, *32*, 3988–3999.
16. Lee, N.; Kim, H.; Choi, S. H.; Park, M.; Kim, D.; Kim, H.-C.; Choi, Y.; Lin, S.; Kim, B. H.; Jung, H. S.; *et al.* Magnetosome-like Ferrimagnetic Iron Oxide Nanocubes for Highly Sensitive MRI of Single Cells and Transplanted Pancreatic Islets. *Proc. Natl. Acad. Sci. U.S.A.* **2011**, *108*, 2662–2667.
17. Bae, K. H.; Park, M.; Do, M. J.; Lee, N.; Ryu, J. H.; Kim, G. W.; Kim, C.; Park, T. G.; Hyeon, T. Chitosan Oligosaccharide-Stabilized Ferrimagnetic Iron Oxide Nanocubes for Magnetically Modulated Cancer Hyperthermia. *ACS Nano* **2012**, *6*, 5266–5273.
18. Alphandéry, E.; Faure, S. P.; Seksek, O.; Guyot, F. O.; Chebbi, I. N. Chains of Magnetosomes Extracted from AMB-1 Magnetotactic Bacteria for Application in Alternative Magnetic Field Cancer Therapy. *ACS Nano* **2011**, *5*, 6279–6296.
19. Guardia, P.; Di Corato, R.; Lartigue, L.; Wilhelm, C.; Espinosa, A.; Garcia-Hernandez, M.; Gazeau, F.; Manna, L.; Pellegrino, T. Water-Soluble Iron Oxide Nanocubes with High Values of Specific Absorption Rate for Cancer Cell Hyperthermia Treatment. *ACS Nano* **2012**, *6*, 3080–3091.
20. Hugounenq, P.; Levy, M.; Alloyeau, D.; Lartigue, L.; Dubois, E.; Cabuil, V.; Ricolleau, C.; Roux, S.; Wilhelm, C.; Gazeau, F.; *et al.* Iron Oxide Monocrystalline Nanoflowers for Highly Efficient Magnetic Hyperthermia. *J. Phys. Chem. C* **2012**, *116*, 15702–15712.
21. Maity, D.; Chandrasekharan, P.; Pradhan, P.; Chuang, K.-H.; Xue, J.-M.; Feng, S.-S.; Ding, J. Novel Synthesis of Superparamagnetic Magnetite Nanoclusters for Biomedical Applications. *J. Mater. Chem.* **2011**, *21*, 14717–14724.
22. Hergt, R.; Dutz, S.; Zeisberger, M. Validity Limits of the Neel Relaxation Model of Magnetic Nanoparticles for Hyperthermia. *Nanotechnology* **2010**, *21*, 015706.
23. Schaller, V.; Wahnström, G.; Sanz-Velasco, A.; Gustafsson, S.; Olsson, E.; Enoksson, P.; Johansson, C. Effective Magnetic Moment of Magnetic Multicore Nanoparticles. *Phys. Rev. B* **2009**, *80*, 092406.
24. Melenev, P.; Rusakov, V.; Raikher, Y. Magnetic Structure of a Spherical Cluster of Monodomain Particles. *Tech. Phys. Lett.* **2008**, *34*, 248–250.
25. Caruntu, D.; Caruntu, G.; Chen, Y.; O'Connor, C. J.; Goloverda, G.; Kolesnichenko, V. L. Synthesis of Variable-Sized Nanocrystals of Fe_3O_4 with High Surface Reactivity. *Chem. Mater.* **2004**, *16*, 5527–5534.
26. Cheng, C.; Xu, F.; Gu, H. Facile Synthesis and Morphology Evolution of Magnetic Iron Oxide Nanoparticles in Different Polyol Processes. *New J. Chem.* **2011**, *35*, 1072–1079.
27. Cabuil, V.; Dubois, E.; Neveu, S.; Bacri, J.; Hasmonay, E.; Perzynski, R. Phase Separation in Aqueous Magnetic Colloidal Solutions. In *Trends in Colloid and Interface Science IX*; Appell, J., Porte, G., Eds.; Springer: Berlin/Heidelberg, 1995; pp 23−29.
28. Bacri, J. C.; Perzynski, R.; Cabuil, V.; Massart, R. Phase Diagram of an Ionic Magnetic Colloid: Experimental Study of the Effect of Ionic Strength. *J. Colloid Interface Sci.* **1989**, *132*, 43–53.
29. Alloyeau, D.; Ricolleau, C.; Oikawa, T.; Langlois, C.; Le Bouar, Y.; Loiseau, A. Comparing Electron Tomography and HRTEM Slicing Methods as Tools To Measure the Thickness of Nanoparticles. *Ultramicroscopy* **2009**, *109*, 788–796.
30. Valamanesh, M.; Langlois, C.; Alloyeau, D.; Lacaze, E.; Ricolleau, C. Combining Moiré Patterns and High Resolution Transmission Electron Microscopy for In-Plane Thin Films Thickness Determination. *Ultramicroscopy* **2011**, *111*, 149–154.
31. Ge, J.; Hu, Y.; Biasini, M.; Beyermann, W. P.; Yin, Y. Superparamagnetic Magnetite Colloidal Nanocrystal Clusters. *Angew. Chem., Int. Ed.* **2007**, *46*, 4342–4345.
32. Levy, M.; Quarta, A.; Espinosa, A.; Figuerola, A.; Wilhelm, C.; García-Hernández, M.; Genovese, A.; Falqui, A.; Alloyeau, D.; Buonsanti, R.; *et al.* Correlating Magneto-Structural Properties to Hyperthermia Performance of Highly Monodisperse Iron Oxide Nanoparticles Prepared by a Seeded-Growth Route. *Chem. Mater.* **2011**, *23*, 4170–4180.
33. Thomas, J. M.; Simpson, E. T.; Kasama, T.; Dunin-Borkowski, R. E. Electron Holography for the Study of Magnetic Nanomaterials. *Acc. Chem. Res.* **2008**, *41*, 665–674.
34. Dunin-Borkowski, R. E.; Kasama, T.; Wei, A.; Tripp, S. L.; Hytch, M. J.; Snoeck, E.; Harrison, R. J.; Putnis, A. Off-Axis Electron Holography of Magnetic Nanowires and Chains, Rings, and Planar Arrays of Magnetic Nanoparticles. *Microsc. Res. Tech.* **2004**, *64*, 390–402.
35. Parker, D.; Lisiecki, I.; Pileni, M. P. Do 8 nm Co Nanocrystals in Long-Range-Ordered Face-Centered Cubic (fcc) Supracrystals Show Superspin Glass Behavior? *J. Phys. Chem. Lett.* **2010**, *1*, 1139–1142.
36. Mamiya, H.; Nakatani, I.; Furubayashi, T. Blocking and Freezing of Magnetic Moments for Iron Nitride Fine Particle Systems. *Phys. Rev. Lett.* **1998**, *80*, 177–180.
37. Parker, D.; Ladieu, F.; Vincent, E.; Meriguet, G.; Dubois, E.; Dupuis, V.; Perzynski, R. Experimental Investigation of Superspin Glass Dynamics. *J. Appl. Phys.* **2005**, *97*, 10A502–10A503.
38. Lartigue, L.; Oh, S.; Prouzet, E.; Guari, Y.; Larionova, J. Superspin-Glass Behavior of $Co_3[Fe(CN)_6]_2$ Prussian Blue Nanoparticles Confined in Mesoporous Silica. *Mater. Chem. Phys.* **2012**, *132*, 438–445.
39. Levy, M.; Gazeau, F.; Bacri, J. C.; Wilhelm, C.; Devaud, M. Modeling Magnetic Nanoparticle Dipole−Dipole Interactions Inside Living Cells. *Phys. Rev. B* **2011**, *84*, 075480.
40. Weddemann, A.; Auge, A.; Kappe, D.; Wittbracht, F.; Hütten, A. Dynamic Simulations of the Dipolar Driven Demagnetization Process of Magnetic Multi-Core Nanoparticles. *J. Magn. Magn. Mater.* **2010**, *322*, 643–646.
41. Dutz, S.; Clement, J. H.; Eberbeck, D.; Gelbrich, T.; Hergt, R.; Müller, R.; Wotschadlo, J.; Zeisberger, M. Ferrofluids of Magnetic Multicore Nanoparticles for Biomedical Applications. *J. Magn. Magn. Mater.* **2009**, *321*, 1501–1504.
42. Levy, M.; Wilhelm, C.; Luciani, N.; Devaux, V.; Gendron, F.; Luciani, A.; Devaud, M.; Gazeau, F. Nanomagnetism Reveals the Intracellular Clustering of Nanoparticles in the Organism. *Nanoscale* **2011**, *3*, 4402–4410.
43. El-Hilo, M.; Chantrell, R. W.; O'Grady, K. A Model of Interaction Effects in Granular Magnetic Solids. *J. Appl. Phys.* **1998**, *84*, 5114–5122.
44. Cabot, A.; Alivisatos, A. P.; Puntes, V. F.; Balcells, L.; Iglesias, Ò.; Labarta, A. Magnetic Domains and Surface Effects in Hollow Maghemite Nanoparticles. *Phys. Rev. B* **2009**, *79*, 094419.

45. Frandsen, C.; Bahl, C. R. H.; Lebech, B.; Lefmann, K.; Kuhn, L. T.; Keller, L.; Andersen, N. H.; von Zimmermann, M.; Johnson, E.; Klausen, S. N.; *et al.* Oriented Attachment and Exchange Coupling of α-Fe_2O_3 Nanoparticles. *Phys. Rev. B* **2005**, *72*, 214406.
46. Bødker, F.; Mørup, S.; Linderoth, S. Surface Effects in Metallic Iron Nanoparticles. *Phys. Rev. Lett.* **1994**, *72*, 282–285.
47. Gazeau, F.; Boué, F.; Dubois, E.; Perzynski, R. Static and Quasi-Elastic Small Angle Neutron Scattering on Biocompatible Ionic Ferrofluids: Magnetic and Hydrodynamic Interactions. *J. Phys.: Condens. Matter* **2003**, *15*, S1305.
48. Gazeau, F.; Bacri, J.-C.; Gendron, F.; Perzynski, R.; Raikher, Y. L.; Stepanov, V. I.; Dubois, E. Magnetic Resonance of Ferrite Nanoparticles: Evidence of Surface Effects. *J. Magn. Magn. Mater.* **1998**, *186*, 175–187.
49. Shilov, V. P.; Bacri, J. C.; Gazeau, F.; Gendron, F.; Perzynski, R.; Raikher, Y. L. Ferromagnetic Resonance in Ferrite Nanoparticles with Uniaxial Surface Anisotropy. *J. Appl. Phys.* **1999**, *85*, 6642–6647.
50. Levy, M.; Wilhelm, C.; Siaugue, J. M.; Horner, O.; Bacri, J.-C.; Gazeau, F. Magnetically Induced Hyperthermia: Size-Dependent Heating Power of Maghemite Nanoparticles. *J. Phys.: Condens. Matter* **2008**, *20*, 204133.
51. Hergt, R. H., R; Zeisberger, M.; Schüler, D.; Heyen, U.; Hilger, I.; Kaiser, W. A. Magnetic Properties of Bacterial Magnetosomes as Potential Diagnostic and Therapeutic Tools. *J. Magn. Magn. Mater.* **2005**, *293*, 80–86.
52. Carrey, J.; Mehdaoui, B.; Respaud, M. Simple Models for Dynamic Hysteresis Loop Calculations of Magnetic Single-Domain Nanoparticles: Application to Magnetic Hyperthermia Optimization. *J. Appl. Phys.* **2011**, *109*, 083921.
53. Lacroix, L.-M.; Malaki, R. B.; Carrey, J.; Lachaize, S.; Respaud, M.; Goya, G. F.; Chaudret, B. Magnetic Hyperthermia in Single-Domain Monodisperse FeCo Nanoparticles: Evidences for Stoner-Wohlfarth Behavior and Large Losses. *J. Appl. Phys.* **2009**, *105*, 023911.
54. Bordelon, D. E.; Cornejo, C.; Gruttner, C.; Westphal, F.; DeWeese, T. L.; Ivkov, R. Magnetic Nanoparticle Heating Efficiency Reveals Magneto-Structural Differences When Characterized with Wide Ranging and High Amplitude Alternating Magnetic Fields. *J. Appl. Phys.* **2011**, *109*, 124904.
55. Burrows, F.; Parker, C.; Evans, R. F. L.; Hancock, Y.; Hovorka, O.; Chantrell, R. W. Energy Losses in Interacting Fine-Particle Magnetic Composites. *J. Phys. D: Appl. Phys.* **2010**, *43*, 474010.
56. Haase, C.; Nowak, U. Role of Dipole–Dipole Interactions for Hyperthermia Heating of Magnetic Nanoparticle Ensembles. *Phys. Rev. B* **2012**, *85*, 045435.
57. Serantes, D.; Baldomir, D.; Martinez-Boubeta, C.; Simeonidis, K.; Angelakeris, M.; Natividad, E.; Castro, M.; Mediano, A.; Chen, D.-X.; Sanchez, A.; *et al.* Influence of Dipolar Interactions on Hyperthermia Properties of Ferromagnetic Particles. *J. Appl. Phys.* **2010**, *108*, 073918.
58. Wilhelm, C.; Gazeau, F.; Bacri, J. C. Magnetophoresis and Ferromagnetic Resonance of Magnetically Labeled Cells. *Eur. Biophys. J.* **2002**, *31*, 118–125.
59. Wilhelm, C.; Gazeau, F. Universal Cell Labelling with Anionic Magnetic Nanoparticles. *Biomaterials* **2008**, *29*, 3161–3174.
60. Wilhelm, C.; Fortin, J. P.; Gazeau, F. Tumour Cell Toxicity of Intracellular Hyperthermia Mediated by Magnetic Nanoparticles. *J Nanosci. Nanotechnol.* **2007**, *7*, 2933–2937.
61. Wilhelm, C.; Billotey, C.; Roger, J.; Pons, J. N.; Bacri, J. C.; Gazeau, F. Intracellular Uptake of Anionic Superparamagnetic Nanoparticles as a Function of Their Surface Coating. *Biomaterials* **2003**, *24*, 1001–1011.
62. Meledandri, C. J.; Brougham, D. F. Low Field Magnetic Resonance Techniques in the Development of Nanomaterials for Biomedical Applications. *Anal. Methods* **2012**, *4*, 331–341.
63. Miguel, O. B.; Gossuin, Y.; Morales, M. P.; Gillis, P.; Muller, R. N.; Veintemillas-Verdaguer, S. Comparative Analysis of the ^{1}H NMR Relaxation Enhancement Produced by Iron Oxide and Core–Shell Iron–Iron Oxide Nanoparticles. *Magn. Reson. Imaging* **2007**, *25*, 1437–1441.
64. Byrne, S. J.; Corr, S. A.; Gun'ko, Y. K.; Kelly, J. M.; Brougham, D. F.; Ghosh, S. Magnetic Nanoparticle Assemblies on Denatured DNA Show Unusual Magnetic Relaxivity and Potential Applications for MRI. *Chem. Commun.* **2004**, 2560–2561.
65. Ghosh, S.; Carty, D.; Clarke, S. P.; Corr, S. A.; Tekoriute, R.; Gun'ko, Y. K.; Brougham, D. F. NMR Studies into Colloidal Stability and Magnetic Order in Fatty Acid Stabilised Aqueous Magnetic Fluids. *Phys. Chem. Chem. Phys.* **2010**, *12*, 14009–14016.
66. Roch, A.; Gossuin, Y.; Muller, R. N.; Gillis, P. Superparamagnetic Colloid Suspensions: Water Magnetic Relaxation and Clustering. *J. Magn. Magn. Mater.* **2005**, *293*, 532–539.
67. McDermott, R.; Lee, S.; Haken, B. T.; Trabesinger, A. H.; Pines, A.; Clarke, J. Microtesla MRI with a Superconducting Quantum Interference Device. *Proc. Natl. Acad. Sci. U.S.A.* **2004**, *101*, 7857–7861.
68. Pöselt, E.; Kloust, H.; Tromsdorf, U.; Janschel, M.; Hahn, C.; Maßlo, C.; Weller, H. Relaxivity Optimization of a PEGylated Iron-Oxide-Based Negative Magnetic Resonance Contrast Agent for T_2-Weighted Spin–Echo Imaging. *ACS Nano* **2012**, *6*, 1619–1624.
69. Paquet, C.; de Haan, H. W.; Leek, D. M.; Lin, H.-Y.; Xiang, B.; Tian, G.; Kell, A.; Simard, B. Clusters of Superparamagnetic Iron Oxide Nanoparticles Encapsulated in a Hydrogel: A Particle Architecture Generating a Synergistic Enhancement of the T_2 Relaxation. *ACS Nano* **2011**, *5*, 3104–3112.
70. Vuong, Q. L.; Berret, J.-F.; Fresnais, J.; Gossuin, Y.; Sandre, O. A Universal Scaling Law To Predict the Efficiency of Magnetic Nanoparticles as MRI T_2-Contrast Agents. *Adv. Healthcare Mater.* **2012**, *1*, 502–512.
71. Ninjbadgar, T.; Brougham, D. F. Epoxy Ring Opening Phase Transfer as a General Route to Water Dispersible Superparamagnetic Fe_3O_4 Nanoparticles and Their Application as Positive MRI Contrast Agents. *Adv. Funct. Mater.* **2011**, *21*, 4769–4775.
72. Taupitz, M.; Schnorr, J.; Abramjuk, C.; Wagner, S.; Pilgrimm, H.; Hünigen, H.; Hamm, B. New Generation of Monomer-Stabilized Very Small Superparamagnetic Iron Oxide Particles (VSOP) as Contrast Medium for MR Angiography: Preclinical Results in Rats and Rabbits. *J. Magn. Reson. Imaging* **2000**, *12*, 905–911.
73. Lee, N.; Choi, Y.; Lee, Y.; Park, M.; Moon, W. K.; Choi, S. H.; Hyeon, T. Water-Dispersible Ferrimagnetic Iron Oxide Nanocubes with Extremely High r_2 Relaxivity for Highly Sensitive *In Vivo* MRI of Tumors. *Nano Lett.* **2012**, *12*, 3127–3131.
74. Ricolleau, C.; Nelayah, J.; Oikawa, T.; Kohno, Y.; Braidy, N.; Wang, G.; Hue, F.; Florea, I.; Pierron Bohnes, V.; Alloyeau, D. Performances of an 80–200 kV Microscope Employing a Cold-FEG and an Aberration-Corrected Objective Lens. *J. Electron Microsc.* DOI: 10.1093/jmicro/dfs072.
75. Ricolleau, C.; Nelayah, J.; Oikawa, T.; Kohno, Y.; Braidy, N.; Wang, G.; Hue, F.; Alloyeau, D. High Resolution Imaging and Spectroscopy Using CS-Corrected TEM with Cold FEG JEM-ARM200F. *JEOL News* **2012**, *47*, 2–8.
76. Gilbert, J. Iterative Methods for the Three-Dimensional Reconstruction of an Object from Projections. *J. Theor. Biol.* **1972**, *36*, 105–117.